Applied Physics A (2020) 126:851
https://doi.org/10.1007/s00339-020-04044-w

Applied Physics A
Materials Science & Processing

Novel p–n junction photocatalyst of BiOCl/$(BiO)_2CO_3$ anchored on RGO with enhanced visible light photocatalytic activity

Y. L. Qin[1,2] · Y. Q. Wang[1,2] · P. Y. Zhao[1,2] · X. Y. Liu[1,2] · Z. Y. Liu[2] · D. R. Ni[2] · B. L. Xiao[2] · Z. Y. Ma[2]

Received: 7 August 2020 / Accepted: 1 October 2020

Abstract
In this study, a novel p–n junction photocatalyst of BiOCl/$(BiO)_2CO_3$ anchored on RGO was synthesized to enhance the visible light photocatalytic activity. The crystal structure and morphology of the prepared samples were characterized via X-ray diffraction (XRD), scanning electron microscope (SEM), X-ray photoelectron spectroscopy (XPS) and Raman spectroscopy, respectively. The photodegradation performances of the samples were evaluated by photodegrading methyl orange (MO) under visible light irradiation. The results showed that nanoparticles of BiOCl/$(BiO)_2CO_3$ were well dispersed on the RGO nanosheets which served as the growth support and the morphology controller. The RGO addition could enhance the photocatalytic performance of the BiOCl/$(BiO)_2CO_3$-RGO composites with the maximum degradation efficiency of 99.1% under visible light irradiation compared to the sample without RGO (80%). The improved property was attributed to the fact that RGO effectively separated the electron–hole pairs of the composites. Meanwhile, the possible mechanism of the photocatalysis was proposed, which revealed the transfer of charge carriers and the formation of active substances in the photocatalytic process.

Keywords Solvothermal method · BiOCl · BiOCl/$(BiO)_2CO_3$ · RGO · Photocatalytic degradation

1 Introduction

As people excessively discharge waste water containing heavy metal ions or organic pollutants, human health is threatened as never before. Therefore, it is urgent to solve water pollution [1]. Traditional methods for treating water pollution are inefficient and costly, and may also produce secondary pollution [2, 3], such as adsorption [4, 5] and ion exchange [6]. Semiconductor photocatalysis technology has the characteristics of high efficiency, environmental protection, stability, and low cost [7, 8]; therefore, it is considered to be an effective water pollution solution [9–11].

Among the numerous semiconductor photocatalysts, BiOCl has attracted lots of attention and great research interest due to its efficient photocatalytic activity, high chemical stability, nontoxicity, and low cost [12]. The two-dimensional (2D) BiOCl nanosheets have a tetragonal structure composed of [Cl–Bi–O–Bi–Cl] sheets, and the electric field is interacted with the chloride ion (Cl^-) by the inner layer $[Bi_2O_2]^{2+}$ through the Coulombic interaction. The structure is favorable for reducing the recombination rate of photogenerated hole–electron pairs [13, 14]. However, the wide bandgap of BiOCl can only use photons in the ultraviolet region, restricting the practical application of BiOCl as a broad-spectrum photocatalyst [14]. Therefore, one of the proposed strategies is to combine BiOCl and $(BiO)_2CO_3$ into a hetero-junction to increase their photocatalytic activity under visible light. $(BiO)_2CO_3$ is a typical oxide associated with Aurivillius and consists of $[Bi_2O_2]^{2+}$ plates staggered between two $(CO_3)^{2-}$ plates. $(BiO)_2CO_3$ has a highly anisotropic internal structure and can promote the formation of sheet-like structures. In particular, the exposed facets have an active role in photocatalysis [15]. Zhang et al. [16] explored that BiOCl/$(BiO)_2CO_3$ prepared by a facile composition-controlled preparation technology showed the

✉ X. Y. Liu
liuxy@imr.ac.cn

✉ Z. Y. Liu
zyliu@imr.ac.cn

[1] School of Science, Shenyang Ligong University, No.6 Nanping Central Road, Shenyang 110159, China

[2] Shi-Changxu Innovation Center for Advanced Materials, Institute of Metal Research, Chinese Academy of Sciences, 72 Wenhua Road, Shenyang 110016, China

Published online: 12 October 2020

best photocatalytic performance than separate BiOCl or $(BiO)_2CO_3$. Meanwhile, Yu et al. [17] reported that BiOCl/$(BiO)_2CO_3$ exhibited better photocatalytic activity toward RhB than P25 (commercial TiO_2) under UV light. Although the photocatalytic performance of BiOCl/$(BiO)_2CO_3$ was improved to some extent, the rapid recombination of electron–hole pairs may still limit the visible light activity of the composites.

Graphene owns a 2D sp^2 carbon network with unique properties, such as the high carrier mobility, optical transparency, and chemical stability [18]. Owing to this unique nanostructure, the photocatalytic performance of the graphene-composite catalysts can be improved. In the present work, we prepared a photocatalyst of BiOCl/$(BiO)_2CO_3$-reduced graphene oxide (BiOCl/$(BiO)_2CO_3$-RGO). A novel heterojunction of p-type BiOCl and n-type $(BiO)_2CO_3$ was first constructed by loading $(BiO)_2CO_3$ nanoparticles on the surface of BiOCl nanosheets via a two-step solvothermal method. Then, the BiOCl/$(BiO)_2CO_3$ was grown on the surface of reduced graphene oxide (RGO) sheets via a hydrothermal method. On the one hand, RGO was expected to promote the separation of electron–hole pairs; on the other hand, the large specific surface area of RGO was expected to improve the adsorption capacity of the material. This paper reported the morphology of the material and also briefly analyzed the improvement of photocatalytic performance.

2 Experimental

2.1 Photocatalysts preparation

All chemicals were of analytical grade and used as received without any further purification. Distilled water was used in all experiments.

2.2 Photocatalyst synthesis

2.2.1 Synthesis of BiOCl/$(BiO)_2CO_3$ nanosheets

Figure 1 shows the flow schematic of the material synthesis process. The $(BiO)_2CO_3$ photocatalyst was prepared as follows: 2 g Na_2CO_3 and 0.3 g cetyltrimethyl bromide (CTAB) were dissolved in 60 ml of deionized water and stirred for 30 min to achieve the solution A. Simultaneously, 1.14 g $Bi(NO_3)_3{\cdot}5H_2O$ and 200 mg citric acid were dissolved in 58 ml deionized water and 2 ml nitric acid, and then stirred magnetically for 30 min to obtain the solution B. Subsequently, the solution B was slowly added into the solution A with constant stirring, and the mixture solution was stirred continuously for 2 h at room temperature. Then, the obtained product was collected by

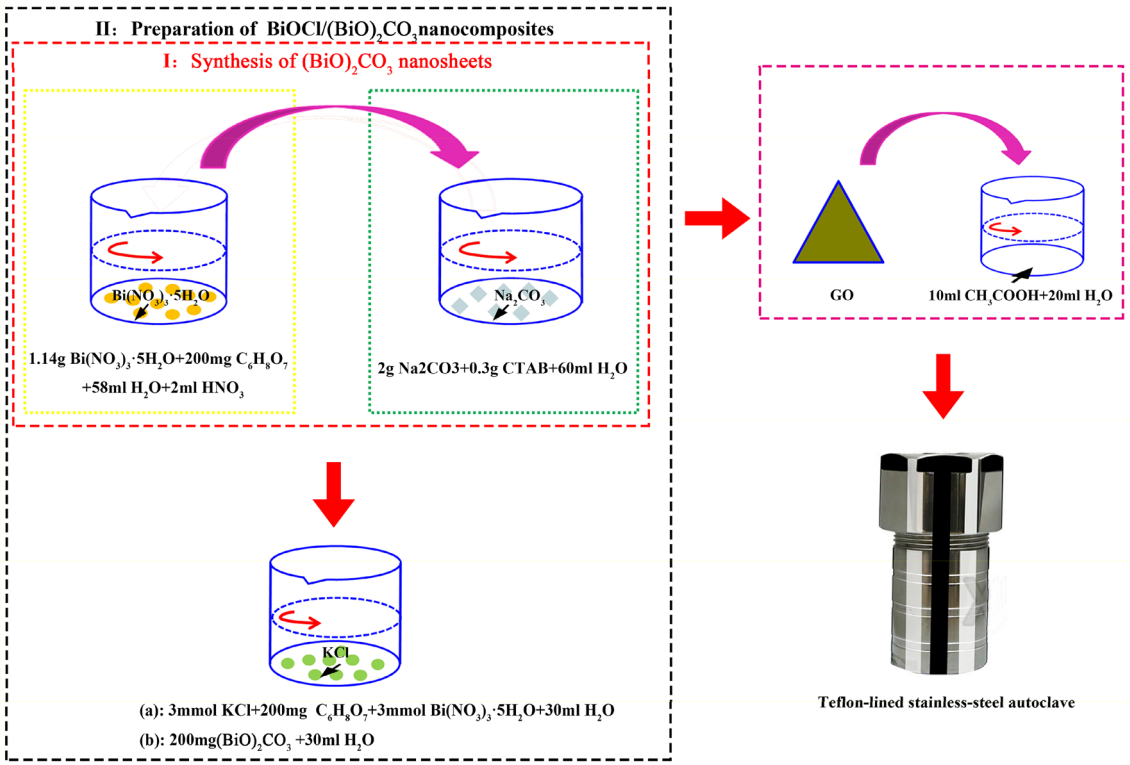

Fig. 1 The flow schematic of the material synthesis process

centrifugation, washed with deionized water and absolute ethanol for several times, and dried at 60 °C for several hours.

BiOCl/$(BiO)_2CO_3$ composites were prepared as follows. First, 3 mmol KCl, 200 mg citric acid and 200 mg $(BiO)_2CO_3$ were dissolved in 30 ml of deionized water and magnetically stirred for 30 min to obtain the solution C. Simultaneously, 3 mmol $Bi(NO_3)_3{\cdot}5H_2O$ was dissolved in 30 ml deionized water and stirred for 30 min, which was labelled as solution D. Then, the solution D was slowly added into the solution C and stirred continuously. The mixture was heated in a water bath at 80 ℃ by magnetic stirring for 3 h. The precipitant was washed several times with deionized water and absolute ethanol, and finally dried in air at 60 ℃.

2.2.2 Preparation of BiOCl/$(BiO)_2CO_3$-RGO nanocomposites

0.01 g graphene oxide (GO) was dispersed in 10 ml ethanol and 20 ml deionized water, following the ultrasonic treatment for 30 min. Next, 0.02 g BiOCl/$(BiO)_2CO_3$ was added into the above reaction mixture by magnetic stirring for 2 h. Then, the obtained mixture was transferred to a 100 ml Teflon-lined stainless-steel autoclave and hydrothermally treated at 160 ℃ for 3 h. After cooling to room temperature naturally, the obtained product was collected and washed thoroughly with deionized water, and then washed with absolute ethanol. Finally, the sample was dried in air at 80 ℃ for 4 h, designated as BiOCl/$(BiO)_2CO_3$-RGO.

2.3 Catalyst characterization

The morphological and structural features of the samples were examined by SUPRA 55 SAPPHIRE field emission scanning electron microscope (SEM) with an acceleration voltage of 15 keV. The crystal phases of the samples were determined by X-ray diffractometry (XRD, Bruker D8 18KW), operating at 40 kV and 50 mA. The XRD testing was conducted using a monochromated Cu K_α radiation ($\lambda = 0.154$ nm), scanned in the range of 10°–80° (2θ) at a scanning rate of 5° min^{-1}. X-ray photoelectron spectroscopy (XPS) was recorded on a VG MultiLab 2000 system with a monochromatic Al Kα source operated at 300 W. Raman spectra of samples were measured on HORIBA with a 532 nm laser at ambient temperature to observe the chemical structures of the samples. The visible light absorption spectra were recorded with a homemade visible light spectrometer.

2.4 Photocatalytic experimental

The photocatalytic activity of the prepared sample was evaluated by monitoring the degradation of the methyl orange (MO) aqueous solution under irradiation of visible light (≥ 420 nm, 500 W xenon lamp) leaving the beaker at 25 cm. In a typical visible light-responsive catalytic process, 30 mg of photocatalyst was dispersed in 50 ml of MO aqueous solution ($c = 20$ mg/L) in a beaker. Before being irradiated, the suspension was magnetically stirred in the dark for 30 min to reach the absorption–desorption equilibrium between the photocatalyst and MO aqueous solution. Then, the solution was exposed to visible light irradiation under magnetic stirring. Then, 4 ml of the suspension was taken every 10 min during the irradiation and centrifuged. The centrifuged solution was recorded at its maximum absorption wavelength. The degradation efficiency was determined by the following equation: $\eta(\%) = \frac{C_0 - C}{C_0} \times 100\%$, where C represents the concentration of MO at each irradiation time, while C_0 represents the starting concentration of MO at initial. MO curve of quasi-first-order kinetic response was measured by the following equation: $kt = \ln\left(\frac{C_0}{C}\right)$, where k is the rate constants, t is the photocatalytic reaction time. Based on the point fitting, the slope of the straight line is the reaction rate constant k.

3 Results and discussion

3.1 Structure and morphology

The Raman spectra of different samples are illustrated in Fig. 2a. The external vibration of carbonate ion in $(BiO)_2CO_3$ caused bands at 179 cm^{-1} and 1070 cm^{-1} [19]. The typical strong peak of BiOCl was located at 145 cm^{-1} corresponded to the A_{1g} internal Bi–Cl stretching mode. The other typical stronger peak was located at 199 cm^{-1} corresponded to the E_g internal Bi–Cl stretching vibration [20]. In general, a slight left shift of the D and G bands of the composite material indicates that GO has been reduced [21, 22]. It can be observed that the peaks at 1357 cm^{-1} (D band) and 1600 cm^{-1} (G band) in the Raman spectrum of GO, respectively, shifted to lower wave numbers of 1353 cm^{-1} and 1593 cm^{-1} in the Raman spectrum of BiOCl/$(BiO)_2CO_3$-RGO, indicating that GO was reduced to RGO. Furthermore, the I_D/I_G value of BiOCl/$(BiO)_2CO_3$-RGO was calculated to be 0.96, which was less than that of GO ($I_D/I_G = 1.05$), implying GO was partly reduced [23, 24].

Figure 2b shows the typical XRD diffraction patterns of the prepared samples. The results showed that all the diffraction peaks can clearly point to the standard diffraction data of tetragonal BiOCl (JCPDS card no. 87-1290) and tetragonal $(BiO)_2CO_3$ (JCPDS card no. 09-0393), respectively, and no other phase or impurity can be observed, indicating that pure tetragonal BiOCl phase and tetragonal $(BiO)_2CO_3$ phase were obtained. For the BiOCl sample, the peaks located at

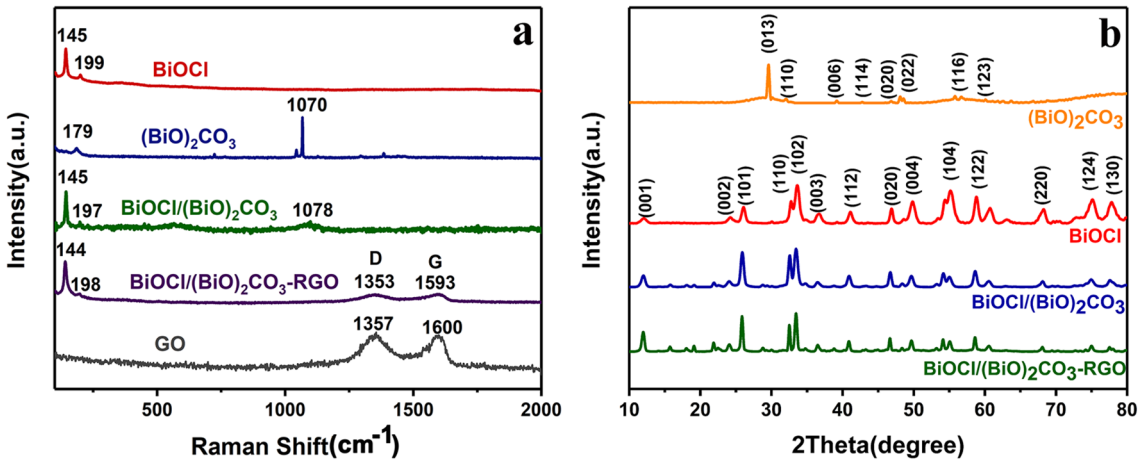

Fig. 2 **a** Raman scattering spectra and **b** XRD patterns of the prepared samples of $(BiO)_2CO_3$, BiOCl, BiOCl/$(BiO)_2CO_3$, and BiOCl/$(BiO)_2CO_3$-RGO

$2\theta = 12.02°$, 24.19° and 26.09° were assigned to the (001), (002) and (101) planes, respectively. It is worth noting that with the addition of $(BiO)_2CO_3$, the (001) peak of BiOCl was significantly enhanced, and the results indicated that $(BiO)_2CO_3$ has been successfully grafted onto BiOCl [25]. Meanwhile, the diffraction intensity ratio of (001)/(101) peaks for the BiOCl/$(BiO)_2CO_3$ and BiOCl/$(BiO)_2CO_3$-RGO were 0.35 and 0.45, respectively. This means that BiOCl/$(BiO)_2CO_3$-RGO had a high percentage of exposure of the (001) surface, indicating that BiOCl grew along the (001) plane. Some researchers reported that the density of oxygen (O) atoms on the (001) plane of bismuth oxychloride was much higher than that on other surfaces [26]. The highly exposed (001) plane promoted the generation of oxygen vacancies, which in turn showed more excellent photocatalytic activity [27]. In addition, the peaks of RGO were not found because the RGO with low atomic number content was small and could not be resolved by XRD [28]. Moreover, the addition of RGO did not change the diffraction peak position of the composites, indicating that RGO did not change the lattice of the BiOCl/$(BiO)_2CO_3$ [29].

The surface composition and chemical state of the prepared samples were further studied via XPS spectra, and the results of the binding energy spectrum were shown in Fig. 3. As shown in Fig. 3a, all the $(BiO)_2CO_3$ (158.3 and 163.6 eV), BiOCl (159 and 164.3 eV), BiOCl/$(BiO)_2CO_3$ (158.9 and 164.2 eV), and BiOCl/$(BiO)_2CO_3$-RGO (159.1 and 164.4 eV) samples had two distinct peaks, respectively, which were indexed to Bi $4f_{7/2}$ and Bi $4f_{5/2}$, respectively. The difference between splitting the two bands was 5.3 eV, indicating the existence of Bi^{3+} [30]. The movement of the characteristic peak position of Bi^{3+} indicated the formation of a heterostructure [31]. In Fig. 3b, The Cl 1*s* of BiOCl can be deconvoluted into two peaks (198.1 and 199.7 eV), designated as Cl $2p_{3/2}$ and Cl $2p_{1/2}$, respectively [14]. It is worth noting that the binding energy of BiOCl/$(BiO)_2CO_3$ and BiOCl/$(BiO)_2CO_3$-RGO became lower, which was related to the introduction of numerous $(BiO)_2CO_3$ [32]. As displayed in Fig. 3c, the double peaks located at 284.5 and 288.1 eV can be assigned to C1*s*. Accidental carbon species vibration in the XPS measurement caused a peak of 284.5 eV [33, 34], while the XPS peak of 288.1 eV was attributed to the carbonate ion in $(BiO)_2CO_3$ [35]. In Fig. 3d, the C 1*s* of the BiOCl/$(BiO)_2CO_3$-RGO XPS spectrum can be deconvoluted into three peaks, appearing at 284.3 (C–C), 285.2 (C–O) and 288.3 eV (C=O); meanwhile, the C–O and C=O peak area ratio decreased greatly. This indicated that the oxygen function was reduced and the sp^2 domain was re-established [36, 37].

The morphology of the prepared samples was analyzed via SEM. Figure 4 showed the SEM images of the pure BiOCl, pure $(BiO)_2CO_3$, BiOCl/$(BiO)_2CO_3$ and BiOCl/$(BiO)_2CO_3$-RGO composites, respectively. As can be seen from Fig. 4a, $(BiO)_2CO_3$ showed morphology of irregular nanoflake and these nanosheets were freely and closely packed with each other. Figure 4b clearly showed that BiOCl was an irregular block structure composed of small nanosheets. As shown in Fig. 4c, when BiOCl was combined with $(BiO)_2CO_3$, the nanosheets of $(BiO)_2CO_3$ were attached to the surface of BiOCl. In Fig. 4d, RGO reduced the agglomeration between the original BiOCl and $(BiO)_2CO_3$, and the BiOCl/$(BiO)_2CO_3$ attached to the surface of the RGO in a sheet shape.

3.2 Photocatalytic performance

The catalytic performance of each catalyst sample for the degradation of MO under visible light is shown in Fig. 5a.

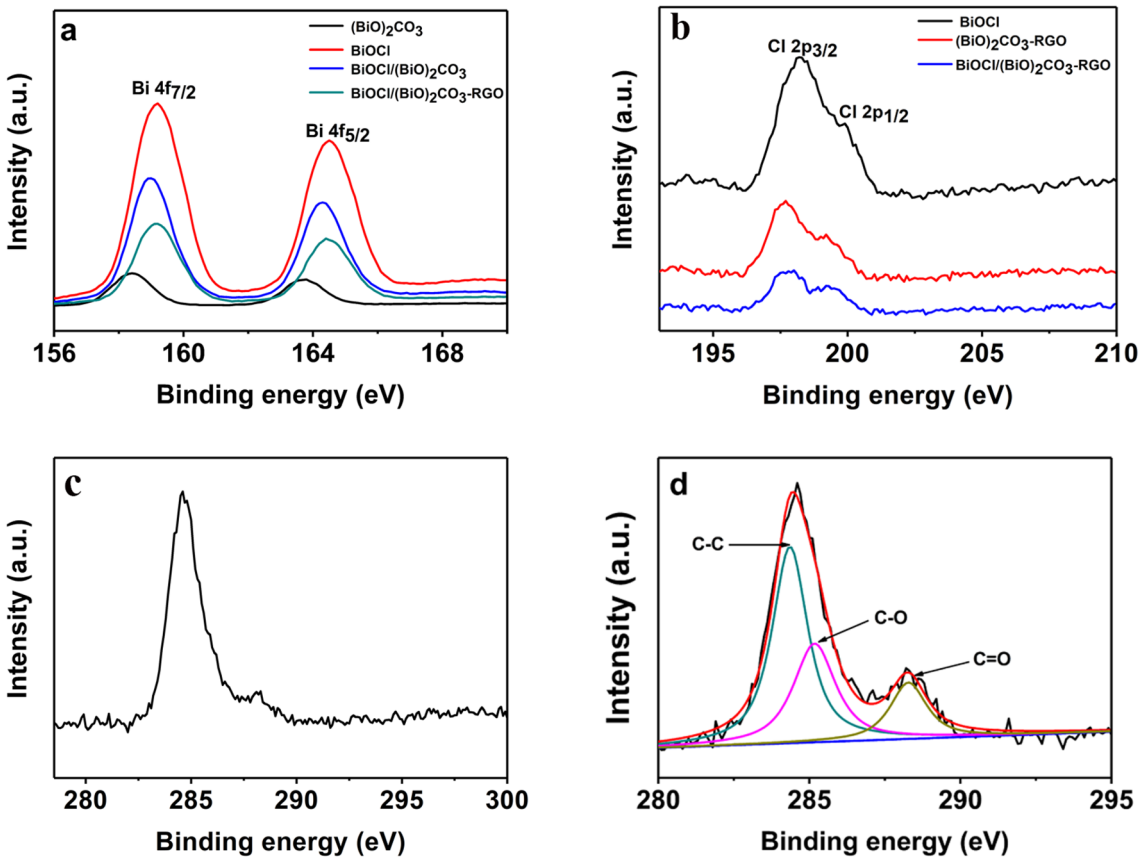

Fig. 3 XPS spectra of **a** Bi 4*f*, **b** Cl 2*p*, **c** C 1*s* of pure $(BiO)_2CO_3$, **d** C 1*s* of BiOCl/$(BiO)_2CO_3$-RGO sample

Within 30 min in the dark, the absorbance decreased by 40% due to adsorption. It can be clearly seen that BiOCl/$(BiO)_2CO_3$-RGO showed the highest photocatalytic performance, and the degradation rate reached 99.2% within 30 min. Obviously, the photocatalytic activity of BiOCl/$(BiO)_2CO_3$-RGO under visible light was better than that of the separate pure $(BiO)_2CO_3$ and BiOCl. This excellent photocatalytic performance is attributed to the fact that RGO reduced the agglomeration of the $(BiO)_2CO_3$ and BiOCl complexes and also positively affected the separation of the composites electron–hole pairs, thus increasing the visible light utilization of the composites [38, 39]. It can be seen from Fig. 5b that BiOCl/$(BiO)_2CO_3$-RGO had the fastest photocatalytic rate, which also proved that BiOCl/$(BiO)_2CO_3$-RGO had the best photocatalytic performance.

3.3 Mechanism for photocatalytic reactions

A possible photocatalytic mechanism for the excellent photocatalytic performance of BiOCl/$(BiO)_2CO_3$-RGO is presented in Fig. 5c. Because $(BiO)_2CO_3$ was a n-type semiconductor while BiOCl was p-type semiconductors [40], p–n junctions would be generated between $(BiO)_2CO_3$ and BiOCl after they contacted with each other, which could effectively separate and transfer photo-generated electrons and holes [41, 42]. N-$(BiO)_2CO_3$ could be excited under visible light ($\lambda > 400$ nm), electrons and holes were produced simultaneously and accumulated on its conduction band (CB) and valence band (VB), respectively. The holes (h^+) from the CB of the n-type $(BiO)_2CO_3$ photocatalyst could be smoothly transferred to the adjacent VB of the p-type BiOCl through the RGO sheets, and the high-speed electron transfer efficiency of the RGO greatly hindered the recombination of electron–hole pairs [43, 44]. The holes could react with OH^- or H_2O species, further generating hydroxyl radicals (·OH) and H_2O_2 with strong oxidative properties to degradation of organics [31]. At the same time, the CB electrons of $(BiO)_2CO_3$ reacted with the oxygen (O_2) adsorbed on the surface of $(BiO)_2CO_3$ to produce a strong oxidant, superoxide (O_2^-), which decomposed organic dyes [45].

It is reported that BiOCl could degrade MO under visible light owing to its photosensitization effect [46]. The MO adsorbed by the BiOCl/$(BiO)_2CO_3$-RGO complex could also be excited (denoted as MO*) under visible light irradiation, producing photo-generated electrons and holes [47]. The excited electrons shifted from the highest occupied molecular

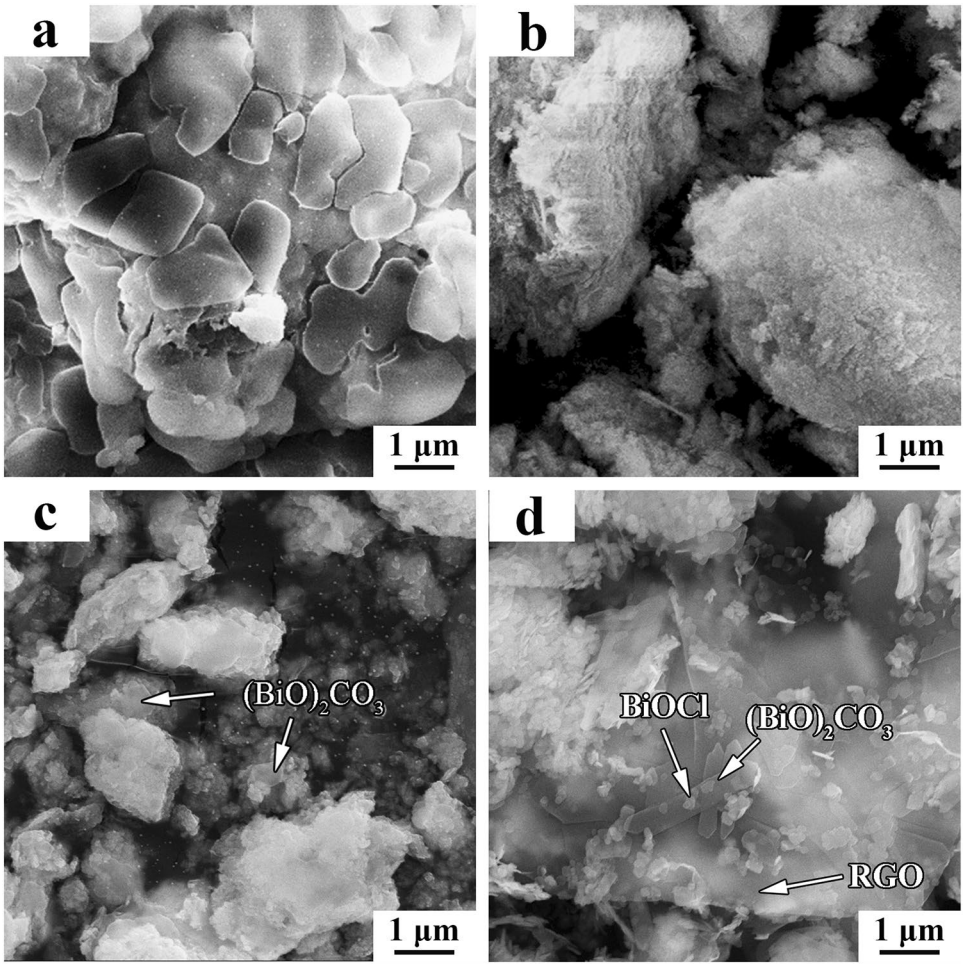

Fig. 4 SEM images of samples: **a** $(BiO)_2CO_3$, **b** BiOCl, **c** $BiOCl/(BiO)_2CO_3$, **d** $BiOCl/(BiO)_2CO_3$-RGO

orbital (HOMO) to the lowest unoccupied molecular orbital (LUMO) [48]. Subsequently, electrons transferred to the CB of BiOCl and then to the CB of $(BiO)_2CO_3$. After that, reactive oxygen species would be produced to further degrade MO. There have been many experiments proving that MO itself could not be degraded under visible light irradiation [49, 50]. This indicates that the photosensitization of the dye was not dominated in the whole catalysis process.

In summary, the main photochemical process steps in the photocatalytic MO mechanism of $BiOCl/(BiO)_2CO_3$-RGO were shown by the following equations:

$$BiOCl/(BiO)_2CO_3 - RGO + h\nu \rightarrow BiOCl/(BiO)_2CO_3 - RGO\ (h^+ + e^-) \quad (1)$$

$$MO + h\nu \rightarrow MO^* + e^- \quad (2)$$

$$O_2 + e^- \rightarrow \bullet O_2^- \quad (3)$$

$$\bullet O_2^- + 2H^+ + e^- \rightarrow H_2O_2 \quad (4)$$

$$H_2O_2 + e^- \rightarrow \bullet OH + OH^- \quad (5)$$

$$h^+ + H_2O \rightarrow \bullet OH + H^+ \quad (6)$$

$$h^+ + OH^- \rightarrow \bullet OH \quad (7)$$

$$MO + \left(\bullet O^{2-}, H_2O_2, \bullet OH\right) \rightarrow \cdots \rightarrow CO_2 + H_2O. \quad (8)$$

4 Conclusion

In summary, $BiOCl/(BiO)_2CO_3$-RGO composites were successfully obtained in a simple solvothermal method to effectively improve the photocatalytic performance. Several conclusions made from this work are as follows:

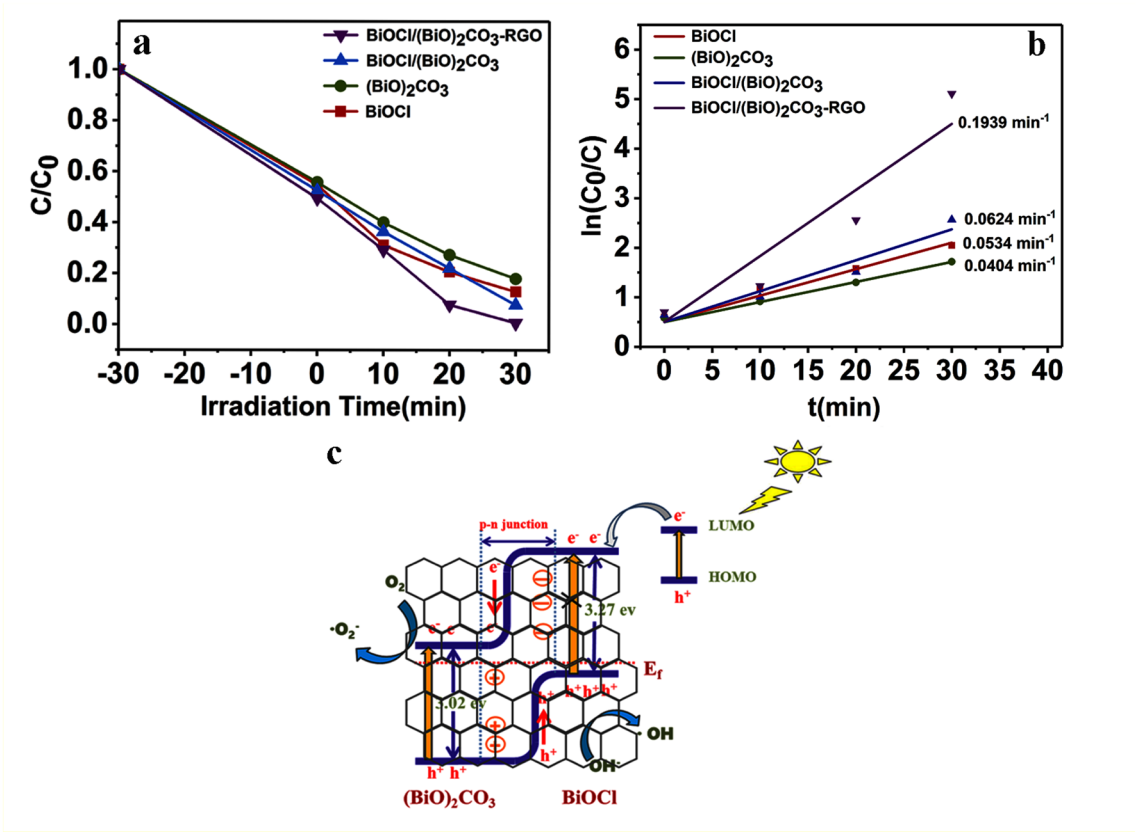

Fig. 5 **a** Photocatalytic degradation curves of MO by samples under visible light irradiation, **b** kinetics of photocatalytic degradation of MO and **c** photocatalytic mechanism of BiOCl/$(BiO)_2CO_3$-RGO under visible light irradiation

(1) BiOCl/$(BiO)_2CO_3$-RGO composites were successfully prepared by hydrothermal method, exhibiting the best photocatalytic performance with a degradation rate reaching 99.2% within 30 min.
(2) Both $(BiO)_2CO_3$ and BiOCl nanosheets were generated in situ on the surface of RGO. A close contact interface was formed between RGO and $(BiO)_2CO_3$ and BiOCl, which could promote efficient separation of electron–hole pairs.
(3) BiOCl/$(BiO)_2CO_3$-RGO composites had a high percentage of exposure of the (001) surface, and promoted the generation of oxygen vacancies. Therefore, it produced more excellent photocatalytic activity.

Acknowledgements The authors gratefully acknowledge the support of: (a) Key Research Program of Frontier Sciences, CAS (no. QYZDJ-SSW-JSC015), (b) the program of Liaoning Education Department (no. LG201605), (c) Key Laboratory Open Fund of Shenyang Ligong University (nos. 4801004yb61-d and 4771004kfs49), (d) the Youth Innovation Promotion Association CAS (2020197).

Author contributions YLQ, YQW and PYZ: contributed equally to this work, and they conceived the idea and designed the experiments; ZYL and XYL: performed the experiments of material preparation; YQW: wrote the paper under the supervision of DRN, BLX and ZYM. All authors participated in the data analysis and discussion.

References

1. L.L. Zhang, A.L. Wang, N. Zhu, B.C. Sun, Y. Liang, W. Wu, Synthesis of butterfly-like $BiVO_4$/RGO nanocomposites and their photocatalytic activities. Chin. J. Chem. Eng. **26**, 667–674 (2018)
2. B. Appavu, S. Thiripuranthagan, S. Ranganathan, E. Erusappan, K. Kannan, $BiVO_4$/N-rGO nano composites as highly efficient visible active photocatalyst for the degradation of dyes and antibiotics in eco system. Ecotoxicol. Environ. Saf. **151**, 118–126 (2018)
3. B. Ou, J.X. Wang, Y. Wu, S. Zhao, Z. Wang, Efficient removal of Cr(VI) by magnetic and recyclable calcined CoFe-LDH/g-C_3N_4 via the synergy of adsorption and photocatalysis under visible light. Chem. Eng. J. **380**, 122600–122612 (2020)
4. N.Y. Zhu, T.M. Yan, J. Qiao, H.L. Cao, Adsorption of arsenic, phosphorus and chromium by bismuth impregnated biochar: adsorption mechanism and depleted adsorbent utilization. Chemosphere **164**, 32–40 (2016)
5. A. Ramirez, R. Ocampo, S. Giraldo, E. Padilla, E. Florez, N. Acelas, Removal of Cr(VI) from an aqueous solution using an activated carbon obtained from teakwood sawdust: kinetics,

equilibrium, and density functional theory calculations. J. Environ. Chem. Eng. **8**, 103702 (2020)
6. W. Beita-Sandí, T. Karanfil, Removal of both *N*-nitrosodimethylamine and trihalomethanes precursors in a single treatment using ion exchange resins. Water Res. **124**, 20–28 (2017)
7. B. Sun, Y.Z. Chen, L. Tao, H.B. Zhao, G.D. Zhao, Y.D. Xia, H.Y. Wang, Y. Zhao, Nanorod array of SnO_2 quantum dot interspersed multiphase TiO_2 heterojunctions with highly photocatalytic water splitting and self-rechargeable battery-like applications. ACS Appl. Mater. Int. **11**, 2071–2081 (2019)
8. T. Zhang, X.T. Zeng, Y.D. Xia, H. Zhang, B. Sun, H.Y. Wang, Y. Zhao, Morphology evolution and photocatalytic applications of W-doped Bi_2O_3 films prepared using unique oblique angle co-sputtering technology. Ceram. Int. **45**, 21968–21974 (2019)
9. S.F. Yin, C.T. Au, H. Li, The charm of photocatalysts. Acta Phys. Chim. Sin. **36**, 1910023 (2020)
10. Y.H. Ni, Y. Kun, F.Y. Xu, W.B. Zhong, Q.H. Zhao, K. Liu, K.L. Yan, D. Wang, Synergistic effect on TiO_2 doped poly(vinyl alcohol-*co*-ethylene) nanofibrous film for filtration and photocatalytic degradation of methylene blue. Compos. Commun. **12**, 112–116 (2019)
11. H. Miyazaki, T. Matsuura, T. Ota, TiO_2 nano-particles based photochromic composite films. Compos. Commun. **10**, 136–139 (2018)
12. Y. Mi, L.Y. Wen, Z.J. Wang, D.W. Cao, R. Xu, Y.G. Fang, Y.L. Zhou, Y. Lei, Fe(III) modified BiOCl ultrathin nanosheet towards high-efficient visible-light photocatalyst. Nano Energy **30**, 109–117 (2016)
13. J.B. Pan, S. Shen, W. Zhou, J. Tang, H.Z. Ding, J.B. Wang, L. Chen, C.T. Au, S.F. Yin, Recent progress in photocatalytic hydrogen evolution. Acta Phys. Chim. Sin. **36**, 1905068 (2020)
14. J.B. Pan, J.J. Liu, S.L. Zuo, U.A. Khan, Y.C. Yu, B.S. Li, Synthesis of cuboid BiOCl nanosheets coupled with CdS quantum dots by region-selective deposition process with enhanced photocatalytic activity. Mater. Res. Bull. **103**, 216–224 (2018)
15. A.J. Wang, J. Zhang, W. Zhao, W.H. Zhu, Q. Zhong, Porphyrin decorated $Bi_2O_2CO_3$ nanocomposites with efficient difunctional properties of photocatalysis and optical nonlinearity. J. Alloy. Compd. **748**, 929–937 (2018)
16. X.C. Zhang, T.Y. Guo, X.W. Wang, Y.W. Wang, C.M. Fan, H. Zhang, Facile composition-controlled preparation and photocatalytic application of BiOCl/$Bi_2O_2CO_3$ nanosheets. Appl. Catal. B Environ. **150**, 486–495 (2014)
17. L.H. Yu, X.Y. Zhang, G.W. Li, Y.T. Cao, Y. Shao, D.Z. Li, Highly efficient $Bi_2O_2CO_3$/BiOCl photocatalyst based on heterojunction with enhanced dye-sensitization under visible light. Appl. Catal. B Environ. **187**, 301–309 (2016)
18. Y.L. Qin, Z. Sun, W.W. Zhao, Z.Y. Liu, D.R. Ni, Z.Y. Ma, Improved photocatalytic properties of ZnS/RGO nanocomposites prepared with GO solution in degrading methyl orange. Nano Struct. Nano Objects **10**, 176–181 (2017)
19. W.D. Zhang, F. Dong, W. Zhang, Capture of atmospheric CO_2 into $(BiO)_2CO_3$/graphene or graphene oxide nanocomposites with enhanced photocatalytic performance. Appl. Surf. Sci. **358**, 75–83 (2015)
20. S. Kang, R.C. Pawar, Y. Pyo, V. Khare, C.S. Lee, Size-controlled BiOCl-RGO composites having enhanced photodegradative properties. J. Exp. Nanosci. **11**, 259–275 (2016)
21. J. Ni, J.J. Xue, L.F. Xie, J. Shen, G.Y. He, H.Q. Chen, Construction of magnetically separable NiAl LDH/Fe_3O_4-RGO nanocomposites with enhanced photocatalytic performance under visible light. Phys. Chem. Chem. Phys. **20**, 414–421 (2018)
22. D.H. Youn, Y.B. Park, J.Y. Kim, G. Magesh, Y.J. Jang, J.S. Lee, One-pot synthesis of NiFe layered double hydroxide/reduced graphene oxide composite as an efficient electrocatalyst for electrochemical and photoelectrochemical water oxidation. J. Power Sources **294**, 437–443 (2015)
23. K.D. Kumar, G.P. Kumar, K.S. Reddy, Rapid microwave synthesis of reduced graphene oxide-supported TiO_2 nanostructures as high performance photocatalyst. Mater. Today Proc. **2**, 3736–3742 (2015)
24. B. Xue, Y.Q. Zou, Uniform distribution of ZnO nanoparticles on the surface of graphene and its enhanced photocatalytic performance. Appl. Surf. Sci. **440**, 1123–1129 (2019)
25. Y.L. Qi, Y.F. Zheng, H.Y. Yin, X.C. Song, Enhanced visible light photocatalytic activity of AgBr on 001 facets exposed to BiOCl. J. Alloy. Compd. **712**, 535–542 (2017)
26. K. Li, Y.J. Liang, J. Yang, Q. Gao, Y.L. Zhu, S.Q. Liu, R. Xu, X.Y. Wu, Controllable synthesis of 001 facet dependent foursquare BiOCl nanosheets: a high efficiency photocatalyst for degradation of methyl orange. J. Alloy. Compd. **695**, 238–249 (2017)
27. M.J. Islam, D.A. Reddy, J. Choi, T.K. Kim, Surface oxygen vacancy assisted electron transfer and shuttling for enhanced photocatalytic activity of a Z-scheme CeO_2–AgI nanocomposite. RSC. Adv. **6**, 19341–19350 (2016)
28. K.S. Divya, A. Chandran, V.N. Reethu, S. Mathew, Enhanced photocatalytic performance of RGO/Ag nanocomposites produced via a facile microwave irradiation for the degradation of Rhodamine B in aqueous solution. Appl. Surf. Sci. **444**, 811–818 (2018)
29. Y.Q. Yang, W.K. Zhang, R.X. Liu, J.M. Cui, C. Deng, Preparation and photocatalytic properties of visible light driven Ag–AgBr-RGO composite. Sep. Purif. Technol. **190**, 278–287 (2018)
30. Y.J. Sun, J.Z. Liao, F. Dong, S.J. Wu, L.D. Sun, A Bi/BiOI/$(BiO)_2CO_3$ heterostructure for enhanced photocatalytic NO removal under visible light. Chin. J. Catal. **40**, 362–370 (2019)
31. L. Gao, X. Li, J.Y. Zhao, X. Zhang, X.H. Zhang, H.T. Yu, In situ preparation of $(BiO)_2CO_3$/BiOBr sheet-on-sheet heterojunctions with enhanced visible light photocatalytic activity. J. Phys. Chem. Solids. **108**, 30–38 (2017)
32. X.Y. Gao, W. Peng, G.B. Tang, Q. Guo, Y.M. Luo, Highly efficient and visible-light-driven BiOCl for photocatalytic degradation of carbamazepine. J. Alloy. Compd. **757**, 455–465 (2018)
33. W.D. Zhang, J. Zhang, F. Dong, Y.X. Zhang, Facile synthesis of in situ phosphorus-doped gC_3N_4 with enhanced visible light photocatalytic property for NO purification. RSC. Adv. **6**, 88085–88089 (2016)
34. G.Q. Zhu, Y.B. Liu, M. Hojamberdiev, J.L. Han, J. Rodríguez, S.A. Bilmes, P. Liu, Thermodecomposition synthesis of porous β-Bi_2O_3/$Bi_2O_2CO_3$ heterostructured photocatalysts with improved visible light photocatalytic activity. New J. Chem. **39**, 9557–9568 (2015)
35. F. Dong, X. Feng, Y.X. Zhang, C.F. Gao, Z.B. Wu, An anion-exchange strategy for 3D hierarchical $(BiO)_2CO_3$/amorphous Bi_2S_3 heterostructures with increased solar absorption and enhanced visible light photocatalysis. RSC. Adv. **5**, 11714–11723 (2015)
36. M. Mitra, S.T. Ahamed, A. Ghosh, A. Mondal, K. Kargupta, S. Ganguly, D. Banerjee, Polyaniline/reduced graphene oxide composite-enhanced visible-light-driven photocatalytic activity for the degradation of organic dyes. ACS Omega **4**, 1623–1635 (2019)
37. T.T. Wang, P. Huang, Y.Q. Li, N. Hu, S.Y. Fu, Epoxy nanocomposites significantly toughened by both poly(sulfone) and graphene oxide. Compos. Commun. **14**, 55–60 (2019)
38. T.Y. Liu, B. Liu, L.F. Yang, X.L. Ma, H. Li, S. Yin, T. Sato, T. Sekino, Y.H. Wang, RGO/Ag_2S/TiO_2 ternary heterojunctions with highly enhanced UV-NIR photocatalytic activity and stability. Appl. Catal. B Environ. **204**, 593–601 (2017)
39. A.H.C. Khavar, G. Moussavi, A.R. Mahjoub, M. Satari, P. Abdolmaleki, Synthesis and visible-light photocatalytic activity of In,

S-TiO_2@rGO nanocomposite for degradation and detoxification of pesticide atrazine in water. Chem. Eng. J. **345**, 300–311 (2018)
40. L. Chen, S.F. Yin, S.L. Luo, R. Huang, Q. Zhang, T. Hong, P.C.T. Au, $Bi_2O_2CO_3$/BiOI photocatalysts with heterojunctions highly efficient for visible-light treatment of dye-containing wastewater. Ind. Eng. Chem. Res. **51**, 6760–6768 (2012)
41. A. Etogo, E. Hu, C.M. Zhou, Y.J. Zhong, Y. Hu, Z.L. Hong, Facile fabrication of mesoporous BiOCl/$(BiO)_2CO_3$/Bi_2O_3 ternary flower-like heterostructured microspheres with high visible-light-driven photoactivity. J. Mater. Chem. A. **3**, 22413–22420 (2015)
42. X. Li, Z.X. Tang, H.D. Ma, F. Wu, R.H. Jian, PVP-assisted hydrothermal synthesis and photocatalytic activity of single-crystalline $BiFeO_3$ nanorods. Appl. Phys. A **125**, 598–604 (2019)
43. M.F.R. Samsudin, A. Mahmood, S. Sufian, Enhanced photocatalytic degradation of wastewater over RGO-TiO_2/$BiVO_4$ photocatalyst under solar light irradiation. J. Mol. Liq. **268**, 26–36 (2018)
44. R. Zhao, X.F. Lu, C. Wang, Electrospinning based all-nano composite materials: recent achievements and perspectives. Compos. Commun. **10**, 140–150 (2018)
45. P. Ahuja, S.K. Ujjain, I. Arora, M. Samim, Hierarchically grown NiO-decorated polyaniline-reduced graphene oxide composite for ultrafast sunlight-driven photocatalysis. ACS Omega **3**, 7846–7855 (2018)
46. T.B. Li, G. Chen, C. Zhou, Z.Y. Shen, R.C. Jin, J.X. Sun, New photocatalyst BiOCl/BiOI composites with highly enhanced visible light photocatalytic performances. Dalton Trans. **40**, 6751–6758 (2011)
47. P. Chowdhury, H. Gomaa, A.K. Ray, Dye-sensitized photocells: a breakthrough in green energy and environmental detoxification. Sustain. Nanotechnol. Environ. Adv. Achiev. **1124**, 231–266 (2013)
48. J. Cao, X. Li, H.L. Lin, B.Y. Xu, S.F. Chen, Q.M. Guan, Surface acid etching of $(BiO)_2CO_3$ to construct $(BiO)_2CO_3$/BiOX (X= Cl, Br, I) heterostructure for methyl orange removal under visible light. Appl. Surf. Sci. **266**, 294–299 (2013)
49. K.J. Lin, J. Qian, Z.H. Zhao, G.L. Wu, H.J. Wu, Synthesis of a carbon-loaded $Bi2O_2CO_3$/TiO_2 photocatalyst with improved photocatalytic degradation of methyl orange dye. J. Nanosci. Nanotechno. **20**, 7653–7658 (2020)
50. J. Divya, N.J. Shivaramu, E. Coetsee, R.E. Kroon, W. Purcell, H.C. Swart, Enhanced luminescence and photocatalytic activity of Bi_2O_3:Ho^{3+} needles. J. Alloy. Compd. **842**, 155641 (2020)